Understanding the potential of Self-Protection Jamming on board of miniature UAVs

Christos V. Ilioudis, Carmine Clemente and John Soraghan
Department of Electronic and Electrical Engineering
University of Strathclyde Glasgow, UK
Email: {c.ilioudis, carmine.clemente, j.soraghan}@strath.ac.uk

Abstract—Unarmed Aerial Vehicle (UAV) systems are very challenging targets due to their small size and ability to fly in low altitudes and speed. Particularly, in radar systems UAVs can exhibit similar radar cross section and Doppler parameters to clutter returns such as birds and trees. For this reason, often the micro-Doppler signature of the detected target is employed as discriminative characteristic. This work aims to examine micro-Doppler jamming solutions that could be implemented on board of miniature UAV platforms in order to deploy electronic countermeasures to radar sensors, with the aim to provide useful information to the radar community to counter these.

Index Terms—Jamming; micro-Doppler; Unarmed Aerial Vehicle; Electronic Warfare.

I. INTRODUCTION

Miniature UAVs, usually refereed to as micro-Drone or simply Drones, have become a target of high importance for both security and defence systems. Even so, Drones are very challenging targets, considered as invisible to the current radars used for air traffic control [1]. There are three main characteristics Drones exhibit that make them hard to monitor, especially when using radar systems. Starting with their physical characteristics, commercial Drones have small size and prevalence of non electrically conductive materials in their structure resulting in low radar reflectivity [2]. Moreover, such platforms are able to fly at low speed and altitude, making them easily to be confused with static or slow-moving clutter such as trees [3]. In addition, Drones are highly manoeuvrable thus confusing tracking algorithms designed for larger air-crafts. These peculiar features have led to the design of radar sensors with specific modes, such as continuous steering and holographic radar in order to deal with the small radar cross section (RCS) and clutter mitigation [4].

Due to their similarities in size and speed with non-manmade targets such as birds and trees, in the literature Drones are mainly discriminated by their *micro-Doppler* signatures [2]. Particularly, a flying Drone can be characterised by two motions: the main motion due to its centre of mass moving from a point to another, and the secondary motions that its rotors blades exhibit. Those secondary motions are generally periodical and introduce secondary Doppler components generally referred to as micro-Doppler effect [5]. Micro-Doppler has been widely used for classification in a variety of targets including ballistic and helicopter targets [6]–[8]. Through the last years, different techniques and system configurations exploiting micro-Doppler have been proposed in the literature for Drone detection and classification [2].

Electronic countermeasures (ECM) are based on intentional emissions designed to interfere with the radar's ability to monitor one or multiple targets. In the literature, numerous ECM techniques have been proposed [9], [10], however they mostly fall into two categories: noise and deceptive jamming. Noise jamming refers to systems that generate interference signals with aim to mask the target's reflected signal completely [9]. In contrast, the objective of deceptive jamming is to modify the transmitted signal in order to confuse the radar into detecting and tracking false targets or even cancelling the reflected signal [10]. Being an important discriminative feature, incorporation of micro-Doppler in deception jamming has been previously investigated in the literature [11]–[14]. Particularly, in [11] the effect of micro-motion feature deception in inverse synthetic aperture images (ISAR) was investigated. In [12] a micro-Doppler jamming signal generation scheme was proposed while simple target examples were also provided. Additionally the authors in [13] and [14] proposed a method of deceptive jamming for tracked vehicles with simulated results comparing the proposed with non micro-motion jamming.

Existing Drone detection solutions on the market are designed assuming that these platforms are not performing electronic counter measures actions to avoid detection. However, this option becomes more realistic with the availability of smaller, lighter and cheaper RF transceivers based on software defined radio (SDR) and that can be easily carried by a Drone. This work aims to examine the capabilities of such ECM systems by proposing a jamming waveform system and investigating its performance through simulations, with the final objective to provide to the radar community an understanding of the counter-measure capabilities that the future generation of miniature UAVs could be able to deploy.

The remainder of the paper is organised as follows. Section II describes the adopted UAV based micro-motion model that will be used in the paper. Section III derives the signal model according to the described target model. In Section IV the proposed deception system is introduced while Section V
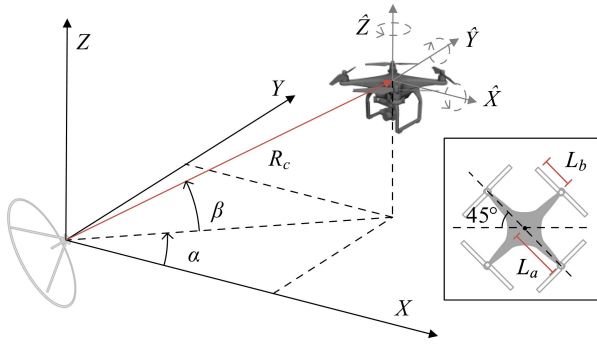
Fig. 1. Geometry of the radar and UAV, and top view of UAV. Overlaid is the sub-reference coordinate system with origin at the target's CM and its axis rotations.
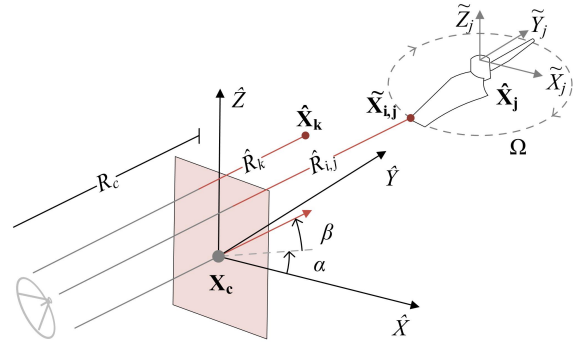

Fig. 2. Target rotor blade (north-east) and overall geometry with the radar signal under far-field assumption.

presents simulation results for different operating scenarios. Finally, Section VI concludes the paper.

II. UAV MICRO-MOTION MODEL

The platform of choice for this analysis is a quad-copter with similar structure to a DJI Phantom 4 [15], while the examined geometry is illustrated in Fig.1. The radar sensor is placed at the axis origin, i.e. $\mathbf{X}_r = [x_r, y_r, z_r] = [0, 0, 0]^T$ while the centre of mass of the UAV target is assumed in an arbitrary position $\mathbf{X}_c = [x_c, y_c, z_c]^T$. The the distance between the radar and the target is therefore given by:

$$R_c = ||\mathbf{X}_c|| \quad (1)$$

where $|| \cdot ||$ denotes the euclidean norm. Additionally, α and β indicate the azimuth and elevation angles of $\mathbf{X}_c$. The top view of the UAV is also shown in Fig.1 where the length of the arm and the one side of the two-sided blade are indicated by L_a and L_b respectively.

Without loss of generality, assume a sub-reference system, $\hat{X}$-$\hat{Y}$-$\hat{Z}$, with axis parallel to the main coordinate system, X-Y-Z, and origin at $\mathbf{X}_c$ (see Fig. 1). The position of each scattering point in the new sub-reference system will depend on the targets morphological properties as well as its orientation. The orientation of the target can be expressed through three 3×3 rotation matrices, $\mathbf{R}_X(\psi), \mathbf{R}_Y(\theta), \mathbf{R}_Z(\phi)$, accounting for the roll, pitch and yaw rotation angles respectively [5]. Being outside of the scope of this paper, the reader is referred to [5] for a complete formulation of these rotation matrices. The initial position of the the j-th rotor in the $\hat{X}$-$\hat{Y}$-$\hat{Z}$ is denoted as $\hat{\mathbf{X}}_j^0$ while the position of any point in the same system can be calculated as:

$$\hat{\mathbf{X}}_k = \mathbf{R}_Z(\phi)\mathbf{R}_Y(\theta)\mathbf{R}_X(\psi)\hat{\mathbf{X}}_k^0 \quad (2)$$

where $\hat{\mathbf{X}}_k^0$ is the position of the k-th point in the $\hat{X}$-$\hat{Y}$-$\hat{Z}$ system.

Furthermore, assume four additional sub-reference coordinate systems centred at the center of rotation of the four double-bladed rotors $\hat{\mathbf{X}}_j^0$. In Fig. 2 one of the sub-reference systems, $\tilde{X}_j$-$\tilde{Y}_j$-$\tilde{Z}_j$, is shown along with the $\hat{X}$-$\hat{Y}$-$\hat{Z}$ axes.

Accounting that the rotor blades can only exhibit rotation on the $\tilde{Z}$ axis, the positions of the scattering points on the j-th blade depend on their initial position and the yaw rotation angle ϕ_j given by:

$$\phi_j = \Omega_j t \quad (3)$$

where Ω_j is the rotation speed of the j-th rotor and t is the time variable. Using (3), the rotation matrix $\mathbf{R}_Z(\phi_j)$ can also be defined. Similar to (2), the position of an i-th arbitrary point on the j-th rotor blade in the $\hat{X}$-$\hat{Y}$-$\hat{Z}$ system is given by:

$$\hat{\mathbf{X}}_{i,j} = \mathbf{R}_Z(\phi)\mathbf{R}_Y(\theta)\mathbf{R}_X(\psi)[\mathbf{R}_Z(\phi_j)\tilde{\mathbf{X}}_{i,j}^0 + \hat{\mathbf{X}}_j^0] \quad (4)$$

where $\tilde{\mathbf{X}}_{i,j}^0$ is the initial position of the scatterer at the $\tilde{X}_j$-$\tilde{Y}_j$-$\tilde{Z}_j$ coordinate system.

Under the far-field assumption, the wave-front can be considered planar instead of spherical [16]. In Fig. 2 the examined geometry is illustrated close to the target. As it can be seen, the distance of a single point on the target from the radar can be approximated as the distance R_c plus the relative distance of the point to the wave-front plane passing from $\mathbf{X}_c$. The relative distance $\hat{R}_k$ (see Fig. 2) can be calculated as:

$$\hat{R}_k = [\mathbf{R}_Y(-\beta)\mathbf{R}_Z(-\alpha)\hat{\mathbf{X}}_k]_x$$
$$= \hat{x}_k \cos\alpha \cos\beta + \hat{y}_k \sin\alpha \cos\beta - \hat{z}_k \sin\beta \quad (5)$$

where $[\cdot]_x$ indicates the x component of the coordinates. This distance can be ether positive or negative depending on if $\hat{\mathbf{X}}_k$ appears before or after the wave-front. The total distance from $\hat{\mathbf{X}}_k$ to $\mathbf{X}_r$ can be approximated as:

$$R_k \approx \hat{R}_k + R_c \quad (6)$$

The distance in (6) will always be positive as $R_c >> |\hat{R}_k|$. Similarly, the distance $R_{i,j}$ from $\hat{\mathbf{X}}_{i,j}$ to $\mathbf{X}_r$ can be calculated from (5) and (6) by replacing $\hat{\mathbf{X}}_k$ with $\hat{\mathbf{X}}_{i,j}$.

III. SIGNAL MODEL

Assume a radar system periodically emitting a waveform with complex envelope $g(t)$ and carrier frequency f_c. The transmitted signal can be expressed as:

$$s(t, u) = g(t)e^{-j2\pi f_c(t+u)} \quad (7)$$

where t is the *fast time* accounting for the time between the beginning and the end of one pulse repetition interval (PRI), i.e. $t \in [T, \mathrm{PRI}]$ where T is the duration of the signal, while u accounts time intervals with duration of a PRI, i.e. $u = 0, \mathrm{PRI}, 2\mathrm{PRI}, ...$, referred to as *slow time*. In the presence of an arbitrary point scatterer m, after pulse compression and carrier removal the signal at the receiver is given by:

$$r_m(t, u) = a_m(u) h_m(t, u) e^{j2\pi f_c \tau_m(u)} \qquad (8)$$

where $a_m(u)$ is the amplitude modulation depending on the radar cross section (RCS) of the scatterer, $h_m(t, u) = g(t - \tau_m(u)) * g(-t)$ is the matched filter output with "$*$" denoting the convolution operator, and $\tau_m(u)$ is the propagation delay due to the relative distance between the radar and the scatterer.

As it can be seen in (8), the time delay is modelled slow-time. Additionally, no Doppler shift is accounted in the fast time as the target is not expected to noticeably change its location during the period of a single pulse [16]. For better understanding it should be also mentioned that $h(t, u)$ contain information related to the range resolution bin that the target falls in the slow time while the complex exponential term is associated with the Doppler of the target.

Accounting for all the target scatterers and the presence of noise, the total received signal is expressed as:

$$r(t, u) = \sum_{k=1}^{K} r_k(t, u) + \sum_{j=1}^{M} \sum_{i=1}^{N} r_{i,j}(t, u) + n(t, u) \qquad (9)$$

where M is the total number of rotor blades, N and K is the number of scatterers on one blade and the main body respectively, and $n(t, u)$ is complex white Gaussian noise $\mathcal{CN}(0, \sigma)$. Additionally, the returns $r_k(t, u)$ and $r_{i,j}(t, u)$ can be calculated from (8) by replacing τ_m with $\tau_k = 2R_k/c$ and $\tau_{i,j} = 2R_{i,j}/c$ respectively, where c is the speed of light and the distances R_k and $R_{i,j}$ are calculated from (6).

IV. DECEPTION SYSTEM

A. System Design

The block diagram of the proposed ECM system is illustrated in Fig. 3. As it can be seen the complete system can be separated in three main parts:

a) Interception: The interception sub-block is associated with capturing and processing the radar signal with focus on two main tasks. First, the receiver shall be the able to perform source localisation operations in order to detect radar sources and estimate their time and direction of arrival. This task is of great significance in cases where false targets are used in the jamming signal. High precision and accuracy are even more important when micro-Doppler signatures are taken into account. Furthermore, the interceptor shall be capable of storing the received signal and identifying key design parameters such as its carrier frequency, complex envelope and PRI. Correct parameters estimation is very important as they will dictate the design of the jamming signal. For example, wrong estimation of the PRI might result in false
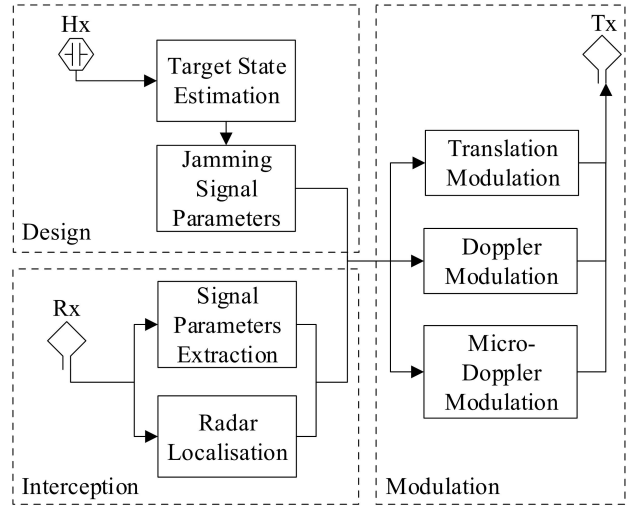

Fig. 3. Block diagram of the proposed ECM system.

targets rapidly changing position making them easier to be discriminated and rejected by the radar.

b) Design: The design sub-block identifies the suitable parameters for the jamming signal. Particularly, on-board sensors will be utilised to extract the target's state parameters such as its velocity, orientation and rotors speed. Such parameters will then be used to estimate the radar signature the target will impose on the intercepted signal. Based on this signature, the proper design characteristics will be then assigned for the jamming signal. Particularly, parameters such as the Doppler spread caused by the rotors can be used to design a jamming signal able to completely cover the micro-Doppler signature of the target. Furthermore, design of false targets could made based on off-line or on-line generated radar signatures which will then be used to update the characteristics of the deception signal.

c) Modulation: In the modulation sub-block, the received radar signal is modulated according to the parameters identified from the interception and design blocks and is then retransmitted. During this process three main modulation are considered. First the translation modulation accounts for changes in the envelope and phase of the signal to account for changes in the location of the projected target. The Doppler modulation will modify the phase of the signal in order to indicate change in the velocity of the centre of mass of the target. Lastly, the micro-Doppler modulation is associated with the micro motion characteristics of the projected target.

B. Jamming Signal

Following the signal model discussed in Section III, the jamming signal for a point target m can be expressed as:

$$q_m(t, u) = \hat{a}_m(u) g(t - \hat{\tau}_m(u)) e^{-j2\pi f_c(t - \hat{\tau}_m(u))} \qquad (10)$$

where $\hat{a}_m(u)$ and $\hat{\tau}_m(u)$ are the designed RCS and delay respectively. Assuming that the radar and jamming signal are received and transmitted from the centre of mass of the target,

TABLE I
LINK BUDGET PARAMETERS

Platform	Description	Parameter	Value	
	Carrier frequency [17]	f_c	1.255	GHz
	Target RCS [18]	σ	0.01	m^2
Radar	Transmitted power [18]	P_T	33	dBW
	Min detectable power	P_D	-40	dBW
	Transmitter gain	G_T	9	dB
	Processing gain [19]	G_P	19.5	dB
	Integration gain	G_I	33.1	dB
	Beamforming gain [17]	G_B	18	dB
	Low noise amplifier gain	G_A	60	dB
	Receiver gain	G_R	130.7	dB
Jammer	Min detectable power	$\hat{P}_\mathrm{D}$	-10	dBW
	Receiver gain	$\hat{G}_\mathrm{J}$	36	dB

Fig. 4. Radar received power from target and jammer transmitted power for a $\mathrm{SIR} = 0\mathrm{dB}$ in different ranges.

from (5) it can be seen that to estimate $\hat{\tau}_m(u)$ the jammer needs the relative potion of m compared to the centre of mass and the direction of arrival of the intercepted signal. Based on (10) the jammer can generate simple, point like targets using one scatterer or more complex targets by combining multiple returns. When multiple returns are considered, proper RCS parameter design is important as different components of the target will induce returns of different intensities, playing a significant role on the final signature.

C. Link budget

As the system is expected to operate under low size weight and power (SWaP) restrictions, the maximum operation range is highly dependent on the ability of the jammer to properly intercept the radar signal and its ability to transmit a powerful enough signal. Additionally, this range shall be longer or close to the maximum detectable range that the radar offers for such a target. The maximum detectable range R_D for a monostatic radar can be calculated through the radar equation:

$$R_\mathrm{D} = \sqrt[4]{\frac{P_\mathrm{T} G_T G_R \lambda^2 \sigma}{(4\pi)^3 P_\mathrm{D}}} \qquad (11)$$

where P_R transmitted power, G_T and G_R are the transmitter and receiver of the radar, $\lambda = c/f_c$ is the wavelength of carrier signal, σ is the total target RCS, P_D is the minimum power required for detection. As a case study, the Aveillant Gamekeeper 16U is used with the chosen parameters being summarised in Table I. Most of the parameters have been drown from [17]–[19] while others have been fixed to offer a maximum detectable range of approximately 5km [18]. The transmitter gain is calculated as $G_\mathrm{T} = 10 \log_{10} N_\mathrm{T}$, where $N_\mathrm{T} = 8$ is the number of transmitting elements [19]. Moreover, the processing gain is calculated as $G_\mathrm{P} = 10 \log_{10} TB$, where $T = 30\mu s$ and $B = 3\mathrm{MHz}$ are the duration and bandwidth of the radar pulse respectively [19]. The integration gain is calculated as $G_\mathrm{I} = 10 \log_{10} N_p$, where $N_p = 2048$ is the number of pulsed used for integration. For a pulse repletion interval $\mathrm{PRF} = 7.5\mathrm{kHz}$ it results to an integration time of
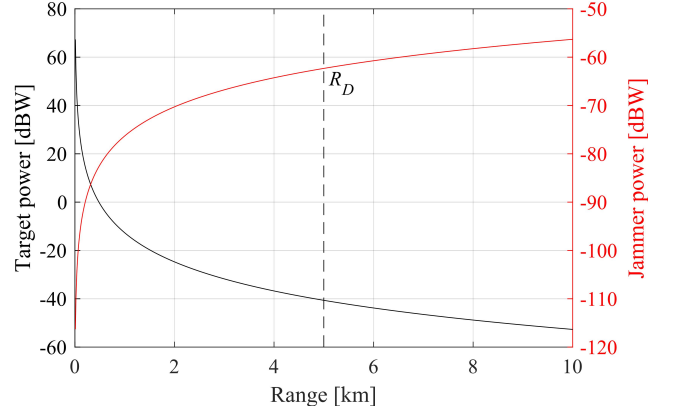
0.28s [19]. The total gain of the receiver G_R is calculated by adding the processing, integration, beamforming and low noise amplifier (LNA) gain. The maximum interception[1] range R_I can be calculated as:

$$R_\mathrm{I} = \sqrt[2]{\frac{P_\mathrm{T} G_\mathrm{T} \hat{G}_\mathrm{R} \lambda^2}{(4\pi)^2 \hat{P}_\mathrm{D}}} \qquad (12)$$

where G_R is the jammer receiver gain and P_D is the minimum received power required for successful interception. From (11) and (12), and using the parameters in Table I, the maximum detectable and interception ranges are given as $R_\mathrm{D} = 4.82\mathrm{km}$ and $R_\mathrm{I} = 5.37\mathrm{km}$ respectively. Therefore, the target will be able to detect the surveillance system approximately from a distance of 0.5km before it gets detected.

Moreover the interference power introduced by the jammer at the radar is given by:

$$P_\mathrm{I} = \frac{\hat{P}_\mathrm{T} G_\mathrm{R} \lambda^2}{(4\pi)^2 R^2} \qquad (13)$$

where $\hat{P}_\mathrm{T}$ and $\hat{G}_\mathrm{T}$ are the transmitted power and gain of the jammer respectively, and R is the distance between the target and the radar. Rearranging (11), in Fig. 4 the received power power by the radar from the target in different range is shown by a black line, with a dashed line indicating the maximum detectable range. Moreover using (13), the red line shows the transmitted by the jammer power $\hat{P}_\mathrm{T}$ in order to achieve a signal to interference (SIR) of 0dB. As it can be seen, close to the detectable range, the jammer has to transmit $-62.5\mathrm{dBW}$ which is also the maximum required power to cancel the reflected signal.

V. SIMULATION RESULTS

Focusing on the micro-Doppler aspect of the target, only returns from the blades are considered. The returns were calculated based on a 3D model of the one side of the blade illustrated in Fig.5. The model comprises 59 triangular

---

[1]The term interception is used to describe successful detection of the radar by the jammer.

Scenario Parameter		Sc. 1	Sc. 2	
Carrier frequency	f_c	10	1.255	GHz
Pulse Repetition Frequency	1/PRI	284	7.2	kHz
Pulse width	T	3.5	30	us
Bandwidth	BW	10	3	MHz
Sampling frequency	f_s	100	45	MHz
Azimuth	α	0	0	deg
Elevation	β	5.7	2.2	deg
Target range	R_c	500	1300	m
Drone Parameter				
Blade length	L_b	120		mm
Arm length	L_a	175		mm
Rotation speed of blades	Ω	733		rad/s
Number of rotors	M	4		
Number of scatterers on blade	N	118		

(a) POFACETS, 1 Single-Blade

(b) Mathematical, One-sided 1 Single-Blade

(c) POFACETS, 4 Double-Blades

(d) Mathematical, 4 Double-Blades

Fig. 6. Spectrogram of the return form Drone rotors simulated for Scenario 1 using the 3D model and POFACETS [20], and a mathematical model [5]; Hamming window of 0.7ms is used with 90% overlap.

faces, each of which representing a scatterer. The RCS of these scatterers is approximated using a Physical optics Facet (POFACETS) prediction model [20]. The parameters used to simulate each scenario are summarised in Table II, see Sc. 1 and Sc.2 for Scenario 1 and Scenario 2 respectively.

A. Scenario 1

In the first scenario, a fixed position target is examined in an X-band and high PRF configuration. While such a scenario might not be representative for long range radars, here it is examined to better access micro-Doppler profile of the target. In Fig.6a the normalised spectrogram of the returns from only one blade from the rotor is illustrated for two rotations. As it can be seen when the blade is moving away from the radar the signal exhibits negative frequency shift while moving towards it results to positive Doppler. Moreover, the signal has different profile depending on the side that the blade is facing the radar. For comparison, the returns simulated using a mathematical model for a rotating blade [5] are illustrated in Fig.6b. The length and width parameters used in the model are similar to the ones extracted by the 3D model. Comparing the two profiles it can be seen that both have the same maximum and minimum frequency shifts, with the mathematical model
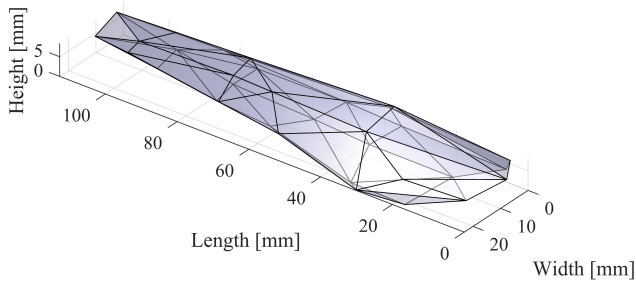

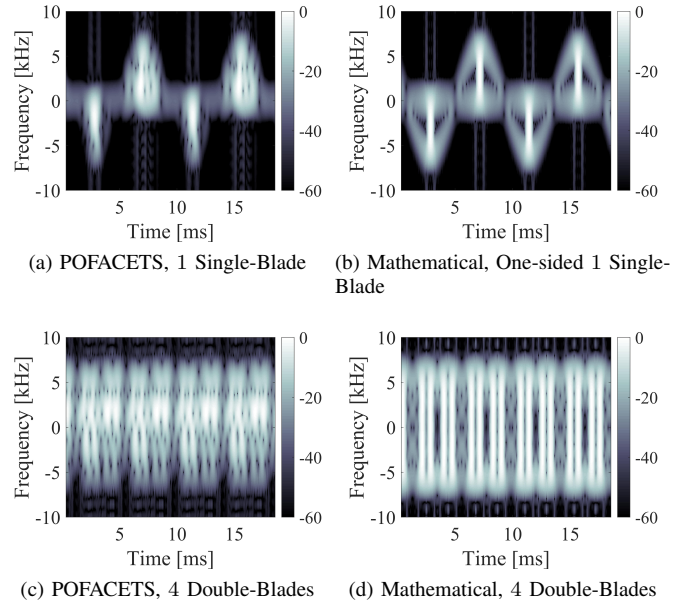Fig. 5. One side blade 3D model used for simulations.

having a pronounced envelope and similar profile for both sides of the blade.

The spectrograms of all 4 double sided rotors are illustrated in Fig. 6c and 6d using the POFACETS and theoretical model respectively. As it can be seen the returns from the different target components overlap in the total range-Doppler profile. The phase of each of these micro-Doppler components will depend on the initial position of the blades and the orientation of the target. Comparing Fig. 6c and 6d it can be seen that the mathematical model results to a fully symmetric micro-Doppler signature along the zero Doppler axis, while the POFACETS is asymmetric. Nevertheless, both cases exhibit similar structure properties such as periodicity and maximum Doppler shift.

B. Scenario 2

In the second scenario initially a stationary drone target is simulated under L-Band and medium PRF configuration. In Fig. 7 the spectrogram of the target returns using POFACETS and theoretical model are illustrated for all 4 double sided blades. Comparing the results with Fig. 6 it can be seen that due to the lower PRF, the individual blade returns are less distinguishable in this scenario. Additionally, since the carrier frequency is also lower in Scenario 2 compared to 1, the maximum Doppler shift has also been reduced. Furthermore, comparing Fig. 7a and 7b it can be seen that both micro-Doppler signatures exhibit very similar characteristics. The respective Range-Doppler (RD) maps generated using a coherent time interval of 0.1s are shown in Fig. 8. As it can be seen, the mathematical model generates a RD profile very similar to the one simulated using POFACETS. Particularly, small differences in intensity of the different frequency component can
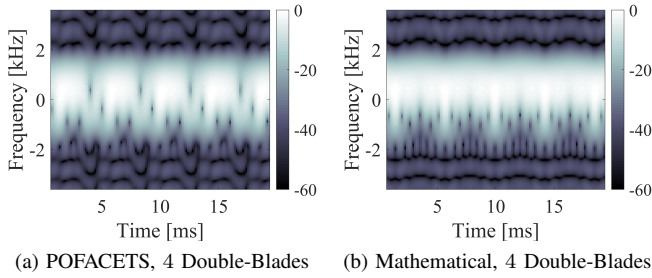
(a) POFACETS, 4 Double-Blades (b) Mathematical, 4 Double-Blades

Fig. 7. Spectrogram of the return form Drone rotors simulated for Scenario 2 using the 3D model and POFACETS [20], and a mathematical model [5]; Hamming window of 1.4ms is used with 90% overlap.
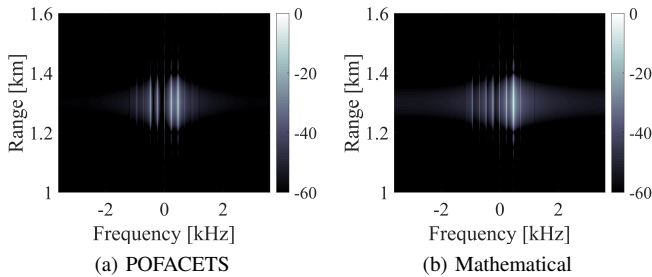

(a) POFACETS (b) Mathematical

Fig. 8. Range-Doppler map of the return form Drone rotors simulated for Scenario 2.

be seen. It should be noted that such differences in intensity will also appear if the initial position of the blades changes and therefore cannot be used as discriminating characteristic for the target.

Evaluating the results from both scenarios, it is demonstrated that using a theoretical model and known operating parameters such as the rotors blades number, length and rotation speed, the target's micro-Doppler signature characteristics can be estimated reliably by the deception system. Additionally, in realistic operating scenarios, using relatively low carrier frequency and PRF, a jammer could be able to generate ghost Drone targets with very similar characteristics to a real target by simply using the theoretical model.

VI. Conclusion

The presented work investigated the potential of ECM in small UAV platforms. Particularly, the appropriate micro-motion model was developed in order to derive a signal model that predicts the micro-Doppler returns from a multirotor miniature UAV target. The model is based on the far-field assumptions and can be used by the jamming system to determine jamming signal parameters such as maximum micro-Doppler shift or generate complex false targets. Additionally, a structure outline for a deception system was proposed in conjunction with a link budget analysis discussing the feasibility and power requirements of such systems. Lastly simulated results based on POFACETS and mathematical models were generated to demonstrate the capabilities of the proposed ECM system in different scenarios. Future plans include the development of the appropriate interception and design algorithms in order

to successfully identify the radar signal and generate the appropriate jamming signal. They outcomes of the research are aimed to help the future radar design to cope with the next generation of drones.

References

[1] A. Haylen and L. Butcher, "Briefing paper on civilian drones," *House of Commons Library*, August 2017.

[2] J. S. Patel, F. Fioranelli, and D. Anderson, "Review of radar classification and rcs characterisation techniques for small uavs or drones," *IET Radar, Sonar Navigation*, vol. 12, no. 9, pp. 911–919, 2018.

[3] R. I. A. Harmanny, J. J. M. de Wit, and G. P. Cabic, "Radar micro-doppler feature extraction using the spectrogram and the cepstrogram," in *2014 11th European Radar Conference*, Oct 2014, pp. 165–168.

[4] M. Jahangir and C. J. Baker, "L-band staring radar performance against micro-drones," in *2018 19th International Radar Symposium (IRS)*. IEEE, 2018, pp. 1–10.

[5] V. Chen, *The Micro-doppler Effect in Radar*, ser. Artech House Remote Sensing Library. Artech House, 2011. [Online]. Available: https://books.google.co.uk/books?id=rE4qmQEACAAJ

[6] A. R. Persico, C. Clemente, D. Gaglione, C. V. Ilioudis, J. Cao, L. Pallotta, A. De Maio, I. Proudler, and J. J. Soraghan, "On model, algorithms, and experiment for micro-doppler-based recognition of ballistic targets," *IEEE Transactions on Aerospace and Electronic Systems*, vol. 53, no. 3, pp. 1088–1108, 2017.

[7] C. Clemente and J. J. Soraghan, "Gnss-based passive bistatic radar for micro-doppler analysis of helicopter rotor blades," *IEEE Transactions on Aerospace and Electronic Systems*, vol. 50, no. 1, pp. 491–500, January 2014.

[8] C. Clemente, T. Parry, G. Galston, P. Hammond, C. Berry, C. Ilioudis, D. Gaglione, and J. J. Soraghan, "Gnss based passive bistatic radar for micro-doppler based classification of helicopters: Experimental validation," in *2015 IEEE Radar Conference (RadarCon)*, May 2015, pp. 1104–1108.

[9] A. De Martino, *Introduction to Modern EW Systems*, ser. Artech House electronic warfare library. Artech House, 2018.

[10] S. Hanbali and R. Kastantin, *A Review of Self-protection Deceptive Jamming Against Chirp Radars*. Cambridge University Press, 2017.

[11] Z. Ben-yu, X. Lei, and B. Da-ping, "A micro-motion feature deception jamming method to isar," in *IEEE 10th INTERNATIONAL CONFERENCE ON SIGNAL PROCESSING PROCEEDINGS*, Oct 2010, pp. 2287–2290.

[12] D. Xue, X. Liu, R. Shen, Z. Liu, and X. Wei, "Micro-motion false target generation in deception jammer against pulse doppler radar," in *2017 IEEE 2nd Advanced Information Technology, Electronic and Automation Control Conference (IAEAC)*, March 2017, pp. 1057–1060.

[13] X. Shi, F. Zhou, B. Zhao, M. Tao, and Z. Zhang, "Deception jamming method based on micro-doppler effect for vehicle target," *IET Radar, Sonar Navigation*, vol. 10, no. 6, pp. 1071–1079, 2016.

[14] X. Shi, F. Zhou, X. Bai, and H. Su, "Deceptive jamming for tracked vehicles based on micro-doppler signatures," *IET Radar, Sonar Navigation*, vol. 12, no. 8, pp. 844–852, 2018.

[15] DJI, "Dji phantom 4 specifications," geodirect.nl/assets/productsheets/DJI-Phantom-4-Datasheet.pdf, Accessed: 2019-05-29.

[16] M. A. Richards, J. A. Scheer, W. A. Holm, B. Beckley, P. Mark, A. Richards *et al.*, "Principles of modern radar volume i-basic principles," 2010.

[17] F. Gersone, A. Balleri, C. J. Baker, and M. Jahangir, "Simulations of l-band staring radar moving target integration efficiency," in *2018 IEEE Conference on Antenna Measurements Applications (CAMA)*, Sep. 2018, pp. 1–4.

[18] A. Ltd, *Gamekeeper 16U Product Sheet*, aveillant.com/files/7515/5559/8083/Gamekeeper_16U.pdf, Accessed: 2019-05-29.

[19] M. Jahangir and C. J. Baker, "Extended dwell doppler characteristics of birds and micro-uas at l-band," in *2017 18th International Radar Symposium (IRS)*, June 2017, pp. 1–10.

[20] F. Chatzigeorgiadis, "Development of code for a physical optics radar cross section prediction and analysis application," NAVAL POSTGRADUATE SCHOOL MONTEREY CA, Tech. Rep., 2004.